Optics Letters

Single pixel polarimetric imaging through scattering media

Kai Ling C. Seow,[1] Peter Török,[2] and Matthew R. Foreman[1,*]

[1]Blackett Laboratory, Department of Physics, Imperial College London, Prince Consort Road, London SW7 2AZ, UK
[2]Division of Physics and Applied Physics, Nanyang Technological University, Singapore, Singapore
*Corresponding author: matthew.foreman@imperial.ac.uk

Received 4 June 2020; revised 2 September 2020; accepted 4 September 2020; posted 8 September 2020 (Doc. ID 399554); published 9 October 2020

Polarimetric imaging can provide valuable information about biological samples in a wide range of applications. Detrimental tissue scattering and depolarization however currently hamper *in vivo* polarization imaging. In this work, single pixel imaging is investigated as a means of reconstructing polarimetric images through scattering media. A theoretical imaging model is presented, and the recovery of the spatially resolved Mueller matrix of a test object behind a scattering phantom is demonstrated experimentally.

https://doi.org/10.1364/OL.399554

Development of quantitative techniques for measurement of biological tissue is vital to improving health care and quality of life. Significant effort has thus been made to improve optical bioimaging technology. Predominantly, current methods are based on measuring optical intensity or wavelength; however, such measurements forego the additional information given by the polarization state of light. Not only does polarization imaging offer additional contrast mechanisms, such as study of birefringence and diattenuation of collagen networks [1], it can also reveal tissue composition and micro-structure [2]. In turn, such information can play a key role in diagnostics and biomedical research, for example, by improving discrimination of cancerous tissues [3], enabling detection of glaucoma [4], and facilitating the study of cartilage diseases [5].

Although *in vivo* bioimaging methods are sought so as to reduce the need for invasive biopsies and histological studies, they are frequently impeded by relatively thick layers of highly scattering tissue that scramble the spatial and polarimetric information contained within an image [6]. Polarization sensitive optical coherence tomography is a well-established polarimetric imaging technique that rejects scattered light by means of coherence and polarization gating [7]. Such methods are, however, typically limited to depths of a transport mean free path (TMFP), approximately 1 mm in biological tissue, due to the decrease in the ballistic intensity for thicker samples. To image deeper, a range of solutions that make use of, rather than reject, scattered light have been proposed for intensity-based imaging modalities, including wavefront shaping, full transmission matrix measurements, use of speckle correlations and single pixel imaging (see Ref. [8] for a review). Polarization information is also known to degrade over longer-length scales [9] and several attempts have thus been made to measure polarization from randomly scattered fields. Recovery of the polarization state of light transmitted through or focused into a scattering medium, for example, has been demonstrated using a speckle correlation scattering matrix approach [10] or broadband wavefront shaping [11], respectively. Although the latter approach has also been used for structural imaging, polarimetric properties of the sample were not retrieved. Vector transmission matrix measurements have also been reported [12], albeit to date their use has been limited to focal field engineering [13].

This Letter aims to demonstrate full polarimetric imaging of a sample through scattering media for the first time to the best of our knowledge. We use a single pixel polarimetric imaging setup [14,15], which combines sequential variation of the illumination and incident polarization state with spatial integration of the polarization resolved output to reconstruct an image [16]. A single pixel polarimetric imaging model and an image reconstruction algorithm are first discussed before a detailed description of a proof-of-principle experimental setup is given. Experimental results of a test object hidden behind scattering phantoms of varying thickness are then presented.

The imaging configuration considered in this work is shown in Fig. 1. A test object, hidden behind a static scattering medium, is illuminated by a coherent spatially modulated beam with a specific input polarization state generated by a polarization state generator (PSG). Light transmitted through the object and scattering medium is then passed through a polarization state analyzer (PSA), which projects the incident light onto a test polarization state, before it is subsequently collected by a single pixel detector. The full polarimetric properties of the object, as described by the spatially dependent Mueller matrix, can then be found using multiple measurements with different input polarization states, analysis states, and illumination profiles.

To model the polarimetric imaging process, consider first discretizing the transverse spatial coordinates into pixels. The field incident on the mth pixel of the object can then be described using the spatially dependent Jones vector $\vec{E}^{\text{inc}}_{mj} = \psi^k_m \vec{E}_j$, where ψ^k_m describes the amplitude modulation of the kth input spatial mode and $\vec{E}_j$ is the Jones vector for the jth input polarization

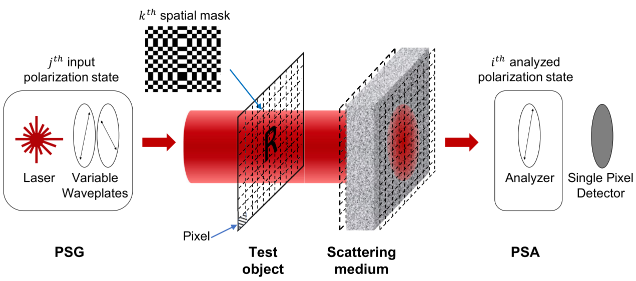

Fig. 1. Schematic of a single pixel polarimetric imaging setup.

state. Letting $\mathbf{T}_m^{\text{obj}}$ denote the Jones matrix of the mth pixel of the object, which is assumed to be thin such that diffraction effects can be neglected, the field at the input surface of the scattering medium is hence $\vec{E}_{mj}^{\text{obj}} = \mathbf{T}_m^{\text{obj}} \vec{E}_{mj}^{\text{inc}}$. Assuming any imaging optics present do not affect the polarization state and that the object is placed immediately before the scattering medium, the Jones vector after the PSA is

$$\vec{E}_{nijk}^{\text{out}} = \mathbf{T}_i \sum_m \mathbf{T}_{nm}^{\text{SM}} \vec{E}_{mj}^{\text{obj}} = \mathbf{T}_i \sum_m \psi_m^k \mathbf{T}_{nm}^{\text{SM}} \mathbf{T}_m^{\text{obj}} \vec{E}_j, \quad \textbf{(1)}$$

where the 2×2 Jones matrix, $\mathbf{T}_{nm}^{\text{SM}}$, relates the Jones vectors at the mth input and nth output pixels and $\mathbf{T}_i$ is the spatially homogenous Jones matrix of the ith PSA.

Since the intensity measured by the single pixel detector is an incoherent sum of the contributions from all output pixels, it is convenient to use the coherency vector representation of light whereby $\vec{C} = \vec{E} \otimes \vec{E}^*$ [17]. In particular, the total spatially integrated coherency vector $\vec{C}_{ijk}^{\text{tot}} = \sum_n \vec{C}_{nijk}^{\text{out}}$ is given by

$$\vec{C}_{ijk}^{\text{tot}} = \sum_m \left(\mathbf{T}_i \otimes \mathbf{T}_i^*\right) \mathbf{A}_m \vec{C}_{mjj}^{\text{obj}} + \sum_m \sum_{l \neq m} \left(\mathbf{T}_i \otimes \mathbf{T}_i^*\right) \mathbf{B}_{ml} \vec{C}_{mlj}^{\text{obj}}, \quad \textbf{(2)}$$

where $\mathbf{A}_m = \mathbf{B}_{mm}$, $\mathbf{B}_{ml} = \sum_n (\mathbf{T}_{nm}^{\text{SM}} \otimes \mathbf{T}_{nl}^{\text{SM},*})$, $\otimes$ denotes the direct product and $*$ represents complex conjugation. No temporal averaging is required since the illumination is coherent and all optical elements are static [17]. Equation (2) shows that the measured coherency vector can be split into two components. The first term is an incoherent sum of contributions from each input pixel, while the second term describes a mixed contribution from different input pixels. In particular, noting that elements in $\mathbf{T}_{nm}^{\text{SM}}$ relate the field components for the mth input and nth output pixels, each element of $\mathbf{B}_{ml}$ represents an estimate of the autocorrelation of output polarized fields as a function of source pixel separation. Typically, this correlation decreases over a length scale κ, which is determined by the smallest of the translation correlation length [18] or the average speckle size [19]. As such, when pixels of a size larger than κ are used, the field from each input pixel gives rise to an uncorrelated output speckle pattern. Accordingly, elements of $\mathbf{A}_m$ are much larger in magnitude than those of $\mathbf{B}_{ml}$ (see Supplement 1), whereby $\vec{C}_{ijk}^{\text{tot}} \approx \sum_m (\mathbf{T}_i \otimes \mathbf{T}_i^*) \mathbf{A}_m \vec{C}_{mjj}^{\text{obj}}$. With a sufficiently large pixel, the total integrated Stokes vector at the detector is hence

$$\vec{S}_{ijk}^{\text{tot}} \approx \mathbf{M}_i \sum_m \mathbf{M}_m^{\text{SM}} \vec{S}_{mjj}^{\text{obj}} = \mathbf{M}_i \sum_m |\psi_m^k|^2 \mathbf{M}_m^{\text{SM}} \mathbf{M}_m^{\text{obj}} \vec{S}_j, \quad \textbf{(3)}$$

where we have used the standard matrix $\boldsymbol{\Gamma}$ to convert between coherency and Stokes vectors ($\vec{S} = \boldsymbol{\Gamma}\vec{C}$), and between Jones and Mueller matrices ($\mathbf{M} = \boldsymbol{\Gamma}(\mathbf{T} \otimes \mathbf{T}^*)\boldsymbol{\Gamma}^{-1}$) [17]. Note that $\vec{S}_j$ is the Stokes vector corresponding to the incident Jones vector $\vec{E}_j$ and that $\mathbf{M}_m^{\text{SM}} = \boldsymbol{\Gamma}\mathbf{A}_m\boldsymbol{\Gamma}^{-1}$.

By definition, the intensity collected by the single pixel detector, I_{ijk}^{tot}, is given by the first element of $\vec{S}_{ijk}^{\text{tot}}$, or explicitly

$$I_{ijk}^{\text{tot}} = \sum_m |\psi_m^k|^2 \left(\vec{a}_i^{\,T} \mathbf{M}_m^{\text{SM}} \mathbf{M}_m^{\text{obj}} \vec{S}_j\right) = \vec{\Psi}_k \cdot \vec{d}_{ij}, \quad \textbf{(4)}$$

where ^{T} denotes transposition and the mth element of the vectors $\vec{\Psi}_k$ and $\vec{d}_{ij}$ correspond to $|\psi_m^k|^2$ and $(\vec{a}_i^{\,T} \mathbf{M}_m^{\text{SM}} \mathbf{M}_m^{\text{obj}} \vec{S}_j)$, respectively. The vector $\vec{a}_i$ is the first row of $\mathbf{M}_i$ and corresponds to the Stokes vector of the ith analyzed polarization state. For each input and analyzed polarization state, the collected intensity is thus seen to be a scalar projection of $\vec{d}_{ij}$ on the spatial mask $\vec{\Psi}_k$. By sequentially projecting spatial masks $\vec{\Psi}_k$, which make up a complete spatial basis, $\vec{d}_{ij}$ can be retrieved using

$$\vec{d}_{ij} = \boldsymbol{\Psi}^{-1} \vec{I}_{ij}^{\text{tot}}, \quad \textbf{(5)}$$

where $\vec{I}_{ij}^{\text{tot}} = [I_{ij1}^{\text{tot}}, I_{ij2}^{\text{tot}}, \ldots]^T$ and $\vec{\Psi}_k$ forms the kth row of the matrix $\boldsymbol{\Psi}$. Once $\vec{d}_{ij}$ is obtained for all input and analyzed polarization states, the set of intensity values for the mth input pixel can be related to the Mueller matrix of the test object, $\mathbf{M}_m^{\text{obj}}$, according to $\mathbf{D}_m = \mathbf{A}\mathbf{M}_m^{\text{SM}}\mathbf{M}_m^{\text{obj}}\mathbf{W}$, where the mth element of $\vec{d}_{ij}$ forms the (i, j)th element of $\mathbf{D}_m$, and the rows (columns) of the so-called instrument matrix $\mathbf{A}$ ($\mathbf{W}$) correspond to the Stokes vectors of the analyzed (input) polarization states, i.e., $\vec{a}_i$ ($\vec{S}_j$). To uniquely determine the 16 elements of $\mathbf{M}_m^{\text{obj}}$, at least four input and analyzed polarization states are required. With suitable PSG and PSA architectures and a known $\mathbf{M}_m^{\text{SM}}$, the spatially resolved Mueller matrix of the object, $\mathbf{M}_m^{\text{obj}}$, can then be computed on a pixel-wise basis as $\mathbf{M}_m^{\text{obj}} = (\mathbf{A}\mathbf{M}_m^{\text{SM}})^{-1}\mathbf{D}_m\mathbf{W}^{-1}$. In practice, however, the presence of noise means that such an inversion typically yields unphysical results. As such, in this work the Mueller matrix of the test object was instead computed using a least squares algorithm (see Supplement 1) that solves for

$$\mathbf{M}_m^{\text{obj}} = \underset{\mathbf{M}}{\text{argmin}} \left\| \mathbf{D}_m - \mathbf{A}\mathbf{M}_m^{\text{SM}}\mathbf{M}\mathbf{W} \right\|_2, \quad \textbf{(6)}$$

subject to the constraint that the related $\mathbf{H}$ matrix is positive semi-definite [20]. In combination, Eqs. (5) and (6) allow the spatially resolved Mueller matrix of the object to be retrieved.

The need to know $\mathbf{M}_m^{\text{SM}}$, i.e., to pre-calibrate the scattering medium, contrasts with conventional intensity based single pixel imaging [16]. Fundamentally, this difference arises since the scattering medium can change the polarization of light such that the total transmittance for each polarization channel differs, whereas for conventional single pixel setups the total transmitted intensity is a fixed proportion of the incident intensity. Two factors, however, can help to mitigate the burden of calibration of $\mathbf{M}_m^{\text{SM}}$. First, many scattering media only introduce an effective depolarization of incident light. Determination of the Mueller matrix then reduces to establishing the corresponding depolarization lengths [9] and medium thickness, which is simpler than a complete Mueller matrix measurement. Second, for a wide-sense statistically homogeneous scattering medium, an ergodic assumption can be made [18]. This implies that if the input pixel is sufficiently large, the measured Mueller matrix is an approximation of the ensemble averaged Mueller matrix because of the spatial averaging. Moreover, $\mathbf{M}_m^{\mathrm{SM}}$ is consequently independent of input pixel location, such that only a single polarimetric measurement is required to determine $\mathbf{M}_m^{\mathrm{SM}}$ for all m. For scattering media that are only piecewise stationary, the associated Mueller matrix for each distinct region would need to be determined. In this work we present results based on the ergodic assumption; however, although not reported here, imaging using the full spatial dependence of $\mathbf{M}_m^{\mathrm{SM}}$ gives comparable results [19].

Using the discussed imaging model, single pixel polarimetric imaging through scattering media was experimentally tested using scattering phantoms made from 1 μm diameter silica microspheres (Merck, Monospher 1000 E) embedded in epoxy resin (Easy Composites GlassCast 50). The fabrication procedure followed closely that discussed by Tahir *et al.* [21]. Biological tissues typically exhibit scattering anisotropy factors close to 1 and mean free paths (MFPs) ∼100 μm [22]. As such, the scattering phantoms were designed to have similar scattering parameters. Taking the refractive indices of the microspheres and cured epoxy resin to be 1.457 and 1.55, respectively, the scattering anisotropy factor of the microspheres was found using Mie theory to be $g = 0.95$. The MFP of the fabricated phantoms was experimentally determined ($l = 395$ μm) by fitting the measured intensity of transmitted ballistic light for phantoms of different thicknesses to the Beer-Lambert law. The corresponding TMFP is $l_{tr} = l/(1-g) = 5$ mm. For the experiments reported here, three scattering media, henceforth referred to as SM1, SM2, and SM3, with $L/l = 18.57, 24.56, 43.13$, respectively ($R = L/l_{tr} = 0.85, 1.12, 1.97$), were used.

The experimental setup used for single pixel polarimetric imaging followed the structure of Fig. 1. The PSG consisted of a laser beam with a wavelength of 638 nm (Cobolt, MLD638) that was passed through a Glan-Thompson prism with its transmission axis oriented in the y direction, followed by two variable waveplates (ARCoptix) oriented at $27 \pm 1°$ and $72 \pm 1°$. Four input polarization states were generated consecutively by applying the phase shifts $(3\pi/4, 3\pi/4)$, $(3\pi/4, 7\pi/4)$, $(7\pi/4, 3\pi/4)$, and $(7\pi/4, 7\pi/4)$. Theoretically, this configuration minimizes the condition number of $\mathbf{W}$ [23], thus reducing noise amplification in the reconstruction algorithm. The beam was then spatially filtered and expanded before it was incident on a digital micromirror device (DMD). The DMD (Texas Instruments, DLP4500) spatially modulated the beam and was imaged onto the object resulting in an effective pixel size of 0.2 mm at the object plane. This pixel size was chosen to be larger than the average speckle size for SM1, thereby satisfying the pixel size requirements discussed above for all phantoms. The object plane was then imaged onto the PSA by a 0.05 numerical aperture lens. Note that the numerical aperture of the lens affects the measurement SNR but not the imaging resolution. When a scattering medium is present, it is placed between the test object and the PSA, such that light transmitted through the phantom is collected. A division of amplitude PSA, analyzing linearly polarized light at x, y, and 45° orientations, as well as left circularly polarized light, was used. The corresponding

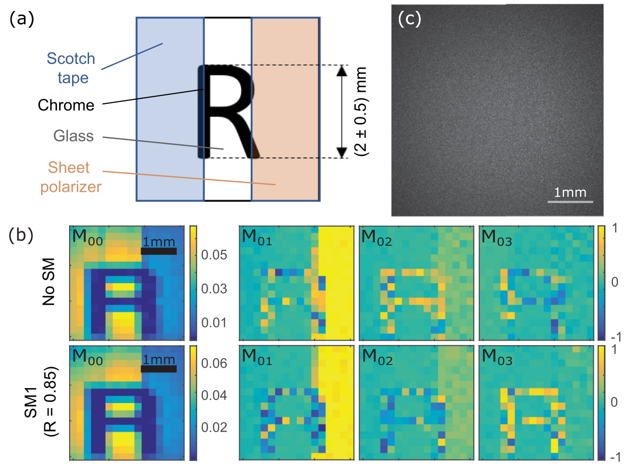

Fig. 2. (a) Illustration of the test object. (b) Comparison of the first row of the spatially resolved Mueller matrix obtained with and without SM1 present. Color scale for M_{00} is in arbitrary units, whereas other Mueller matrix elements are normalized by the unpolarized transmittance (M_{00}). Discrepancies seen in low transmittance pixels, comprising the opaque letter R, are due to noise amplification during normalization. (c) Image taken by a CMOS camera.

theoretical condition number of $\mathbf{A}$ is 3.23. Although PSAs with lower condition numbers are possible [24], the chosen setup can be built economically. To enhance the signal-to-noise ratio (SNR), lock-in detection was also implemented by modulating the intensity of the laser source using a frequency generator (TTi, TG330) and sequentially forwarding the measured signal from the four detectors into a lock-in amplifier (Stanford Research Systems, Model SR530).

An illustration of the test object used is shown in Fig. 2(a). It consisted of the letter R printed on a soda lime glass substrate using low-reflectivity chrome (Thorlabs, R1L3S3P) with a sheet polarizer (Thorlabs, LPVISE2X2) and scotch–tape adhered to distinct regions. The transmission axis of the sheet polarizer was oriented in the x direction. This test object possesses both a spatial variation in polarimetric properties (i.e., polarizer, glass, and retarder) as well as transmittance (i.e., the opaque letter R). Before any measurements were made, the instrument matrices, $\mathbf{A}$ and $\mathbf{W}$, were obtained using the eigenvalue calibration method [25]. A single measurement of $\mathbf{M}_m^{\mathrm{SM}}$ was subsequently taken for each scattering medium without the test object present. Specifically, the entire scattering medium was uniformly illuminated, and measurements were taken for each input and analyzed polarization state. $\mathbf{M}_m^{\mathrm{SM}}$ was then found using a constrained minimum least squares algorithm analogous to that above. Validation of the setup can be found in Ref. [19].

Upon insertion of the test object, image data was acquired by sequentially displaying spatial masks from a scrambled Hadamard basis of order 16 [26] on the DMD for each input polarization state. The corresponding intensities recorded by the photodiodes were processed for each scattering medium using Eqs. (5) and (6) to recover $\mathbf{M}_m^{\mathrm{obj}}$. The reconstructed images obtained with and without SM1 present are shown in Fig. 2(b). For brevity, only the first row of the spatially resolved Mueller matrices are presented. Full Mueller matrices for all three scattering media can be found in Supplement 1. M_{00} is shown in its original form to highlight reconstruction of the object's unpolarized transmittance; however, the remaining elements are normalized by their respective M_{00} values so as to discriminate the polarimetric properties of each pixel more easily. Qualitatively, it can be seen that the Mueller matrix obtained with and without SM1 present are very similar. In contrast, an image taken with a complementary metal–oxide–semiconductor (CMOS) camera [Fig. 2(c)] exhibits a speckle pattern with no correspondence to the test object.

The difference between the matrix elements of the normalized Mueller matrices obtained with and without each scattering medium present was quantified by computing the root-mean-squared error (RMSE) for each normalized Mueller matrix element across all image pixels (Fig. 3). Pixels related to the opaque letter R (found via thresholding the M_{00} matrix element) consist primarily of noise that was further amplified upon normalization, and hence were excluded when computing the RMSE. It can be seen that the average RMSE was ≈ 0.1 for SM1 and SM2, but increased to ≈ 0.3 for SM3. The increase in the RMSE reflects the larger depolarization caused by thicker media and the decrease in the SNR at greater thicknesses. The latter occurs because more light is scattered out of the collection angle of the PSA. For example, the total intensity transmitted through SM3 was 85% lower than that of SM1 for the first analyzed and input polarization state. Consequently, the reconstructed images were visibly noisier for thicker phantoms, as evident in Fig. 4. Nevertheless, polarimetric information was still recoverable even for SM3. For instance, note that the first row of the Mueller matrix of an ideal linear polarizer with its transmission axis oriented in the x direction is [1,1,0,0]. By comparison, for scotch–tape and the glass substrate it is theoretically [1,0,0,0]. The right-hand region of the object, corresponding to the linear polarizer, can be clearly distinguished in Fig. 4. The full Mueller matrix presented in Supplement 1 shows that all three materials in the test object can be well distinguished.

In summary, this work has demonstrated single pixel polarimetric imaging through scattering media. Using a proposed imaging model, it was shown that under coherent illumination, single pixel polarimetric imaging through scattering media was possible for pixel sizes larger than the spatial correlation length of the scattering medium for which contributions from different input pixels sum incoherently. This was further demonstrated in experiments in which the spatially resolved Mueller matrix of a test object hidden behind scattering phantoms with thicknesses up to twice the TMFP was reconstructed. As with most techniques, the imaging depth of single pixel polarimetric imaging is mainly limited by the decrease in the SNR as the thickness of the scattering medium increases. Nevertheless, the utilization of scattered light has enabled imaging at greater depths than imaging with ballistic light alone.

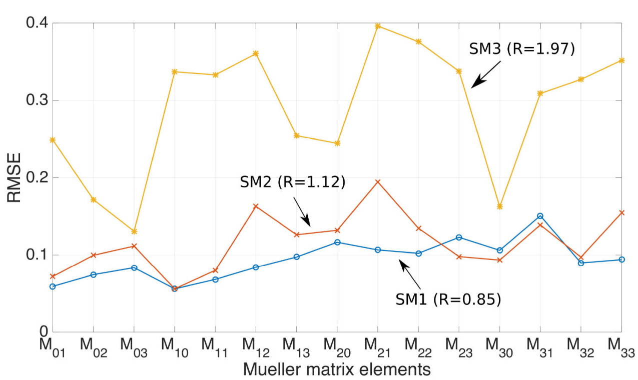

Fig. 3. RMSE for the normalized Mueller matrix elements.

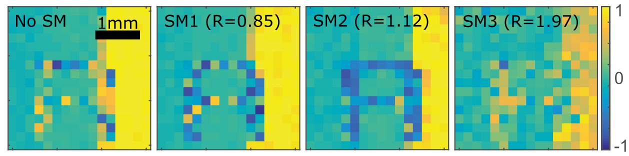

Fig. 4. Normalized M_{01} element of the Mueller matrix obtained for imaging through different scattering media.

Funding. DSO National Laboratories–Singapore; Royal Society.

Disclosures. The authors declare no conflicts of interest.

See Supplement 1 for supporting content.

REFERENCES

1. J. Chue-Sang, Y. Bai, S. Stoff, M. Gonzalez, N. Holness, J. Gomes, R. Jung, A. Gandjbakhche, V. V. Chernomordik, and J. C. Ramella-Roman, J. Biomed. Opt. **22**, 086010 (2017).
2. N. Mazumder, C.-W. Hu, J. Qiu, M. R. Foreman, C. Macías-Romero, P. Török, and F.-J. Kao, Methods **66**, 237 (2014).
3. T. Novikova, A. Pierangelo, A. De Martino, A. Benali, and P. Validire, Opt. Photon. News **23**(10), 26 (2012).
4. T. Dada, R. Sharma, D. Angmo, G. Sinha, S. Bhartiya, S. K. Mishra, A. Panda, and R. Sihota, Indian J. Ophthalmol. **62**, 1045 (2014).
5. P. G. Ellingsen, M. B. Lilledahl, L. M. S. Aas, C. D. L. Davies, and M. Kildemo, J. Biomed. Opt. **16**, 116002 (2011).
6. N. Byrnes and M. R. Foreman, New J. Phys. **22**, 083023 (2020).
7. J. F. de Boer, C. K. Hitzenberger, and Y. Yasuno, Biomed. Opt. Express **8**, 1838 (2017).
8. S. Yoon, M. Kim, M. Jang, Y. Choi, W. Choi, S. Kang, and W. Choi, Nat. Rev. Phys. **2**, 141 (2020).
9. V. Sankaran, K. Schönenberger, J. T. Walsh, and D. J. Maitland, Appl. Opt. **38**, 4252 (1999).
10. K. Lee and Y. Park, Phys. Rev. Appl. **12**, 024003 (2019).
11. H. B. de Aguiar, S. Gigan, and S. Brasselet, Sci. Adv. **3**, e1600743 (2017).
12. S. Tripathi, R. Paxman, T. Bifano, and K. C. Toussaint, Opt. Express **20**, 16067 (2012).
13. Y. Guan, O. Katz, E. Small, J. Zhou, and Y. Silberberg, Opt. Lett. **37**, 4663 (2012).
14. F. Soldevila, E. Irles, V. Duran, P. Clemente, M. Fernandez-Alonso, E. Tajahuerce, and J. Lancis, Appl. Phys. B **113**, 551 (2013).
15. S. Kim, B. Cense, and C. Joo, Opt. Lett. **45**, 3965 (2020).
16. E. Tajahuerce, V. Durán, P. Clemente, E. Irles, F. Soldevila, P. Andrés, and J. Lancis, Opt. Express **22**, 16945 (2014).
17. R. Azzam and N. M. Bashara, *Ellipsometry and Polarized Light* (North-Holland, 1977).
18. B. Judkewitz, R. Horstmeyer, I. M. Vellekoop, I. N. Papadopoulos, and C. Yang, Nat. Phys. **11**, 684 (2015).
19. K. Seow, "Single pixel polarimetric imaging through scattering media," Ph.D. thesis (Imperial College London, 2020).
20. J. J. Gil, J. Opt. Soc. Am. A **17**, 328 (2000).
21. K. Tahir and C. Dainty, J. Opt. A **7**, 207 (2005).
22. V. Ntziachristos, Nat. Methods **7**, 603 (2010).
23. A. De Martino, Y.-K. Kim, E. Garcia-Caurel, B. Laude, and B. Drévillon, Opt. Lett. **28**, 616 (2003).
24. M. R. Foreman, A. Favaro, and A. Aiello, Phys. Rev. Lett. **115**, 263901 (2015).
25. E. Compain, S. Poirier, and B. Drevillon, Appl. Opt. **38**, 3490 (1999).
26. T. T. Do, L. Gan, N. H. Nguyen, and T. D. Tran, IEEE Trans. Signal Process. **60**, 139 (2012).